Design, performance, and grounding aspects of the International Thermonuclear Experimental Reactor ion cyclotron range of frequencies antenna
Durodié F, Dumortier P, Vrancken M, Messiaen A, Bamber R, Hancock D, Huygen S, Lockley D, Louche F, Maggiora R, Milanesio D, Nightingale M P S, Shannon M, Tigwell P, Van Schoor M, Vervier M, Wilson D, Winkler K, CYCLE Team

AIP | Physics of Plasmas

Design, performance, and grounding aspects of the International Thermonuclear Experimental Reactor ion cyclotron range of frequencies antenna

F. Durodié, P. Dumortier, M. Vrancken, A. Messiaen, R. Bamber, D. Hancock, S. Huygen, D. Lockley, F. Louche, R. Maggiora, D. Milanesio, M. P. S. Nightingale, M. Shannon, P. Tigwell, M. Van Schoor, M. Vervier, D. Wilson, K. Winkler, and CYCLE Team

Citation: Physics of Plasmas (1994-present) **21**, 061512 (2014); doi: 10.1063/1.4884379
View online: http://dx.doi.org/10.1063/1.4884379
View Table of Contents: http://scitation.aip.org/content/aip/journal/pop/21/6?ver=pdfcov
Published by the AIP Publishing

Design, performance, and grounding aspects of the International Thermonuclear Experimental Reactor ion cyclotron range of frequencies antenna

F. Durodié,[1,a)] P. Dumortier,[1] M. Vrancken,[1] A. Messiaen,[1] R. Bamber,[2] D. Hancock,[2] S. Huygen,[1] D. Lockley,[2] F. Louche,[1] R. Maggiora,[3] D. Milanesio,[3] M. P. S. Nightingale,[2] M. Shannon,[2] P. Tigwell,[2] M. Van Schoor,[1] M. Vervier,[1] D. Wilson,[2] K. Winkler,[4] and CYCLE Team[b)]

[1]*LPP-ERM/KMS, Association EURATOM-Belgian State, Brussels, Belgium*
[2]*EURATOM/CCFE Assoc., Culham Science Centre, Abingdon OX14 3DB, United Kingdom*
[3]*Associazione EURATOM-ENEA, Politechnico di Torino, Italy*
[4]*IPP-MPI, EURATOM-Assoziation, Garching, Germany*

(Received 19 November 2013; accepted 6 February 2014; published online 24 June 2014)

ITER's Ion Cyclotron Range of Frequencies (ICRF) system [Lamalle *et al.*, Fusion Eng. Des. **88**, 517–520 (2013)] comprises two antenna launchers designed by CYCLE (a consortium of European associations listed in the author affiliations above) on behalf of ITER Organisation (IO), each inserted as a Port Plug (PP) into one of ITER's Vacuum Vessel (VV) ports. Each launcher is an array of 4 toroidal by 6 poloidal RF current straps specified to couple up to 20 MW in total to the plasma in the frequency range of 40 to 55 MHz but limited to a maximum system voltage of 45 kV and limits on RF electric fields depending on their location and direction with respect to, respectively, the torus vacuum and the toroidal magnetic field. A crucial aspect of coupling ICRF power to plasmas is the knowledge of the plasma density profiles in the Scrape-Off Layer (SOL) and the location of the RF current straps with respect to the SOL. The launcher layout and details were optimized and its performance estimated for a worst case SOL provided by the IO. The paper summarizes the estimated performance obtained within the operational parameter space specified by IO. Aspects of the RF grounding of the whole antenna PP to the VV port and the effect of the voids between the PP and the Blanket Shielding Modules (BSM) surrounding the antenna front are discussed. These blanket modules, whose dimensions are of the order of the ICRF wavelengths, together with the clearance gaps between them will constitute a corrugated structure which will interact with the electromagnetic waves launched by ICRF antennas. The conditions in which the grooves constituted by the clearance gaps between the blanket modules can become resonant are studied. Simple analytical models and numerical simulations show that mushroom type structures (with larger gaps at the back than at the front) can bring down the resonance frequencies, which could lead to large voltages in the gaps between the blanket modules and perturb the RF properties of the antenna if they are in the ICRF operating range. The effect on the wave propagation along the wall structure, which is acting as a spatially periodic (toroidally and poloidally) corrugated structure, and hence constitutes a slow wave structure modifying the wall boundary condition, is examined. © *2014 AIP Publishing LLC*. [http://dx.doi.org/10.1063/1.4884379]

I. INTRODUCTION

The design of the ITER Ion Cyclotron Range of Frequencies (ICRF)[1] launcher is supported by the results obtained with the ITER-Like Antenna on JET in 2008–2009 (Ref. 2) which validate the TOPICA[3,4] coupling estimations; demonstrate that there were no unforeseen difficulties in operating up to 42 kV (which was not a limit); achieved power densities in the range required by ITER in terms of reliability and did not result in excessive ICRF impurity production.

Additional confirmation of the proposed matching and its load resilient operation were also demonstrated on ELMy plasmas on JET's A2 ICRF antennas.[5,6]

Fig. 1 shows a poloidal section of 1 of 8 similar sub-assemblies arranged in a 2 poloidal by 4 toroidal array making up the whole array and its CST Microwave Studio (CST-MWS)[7] 3D RF model where the outer conductors have been left out.

II. RF OPTIMIZATION AND ESTIMATED PERFORMANCE

ITER ICRF antenna's capability to couple power to plasma is determined by: the plasma Scrape-Off Layer (SOL) location and profiles;[8] the shaping of the front strap array, organized as a 6 poloidal by 4 toroidal array of short straps; the overall layout of the feed network and the detailed design of its RF components. The first two factors are taken into account in the strap array 24x24 scattering matrix, S_{24}, or impedance matrix, Z_{24}, calculated by TOPICA by importing a CAD model of front face of the antenna and using

[a)]Electronic mail: frederic.durodie@rma.ac.be
[b)]CYCLE consortium of research institutes listed in the affiliations above including "Association Euratom-CEA, CEA, IRFM, 13108 St Paul lez Durance, France."

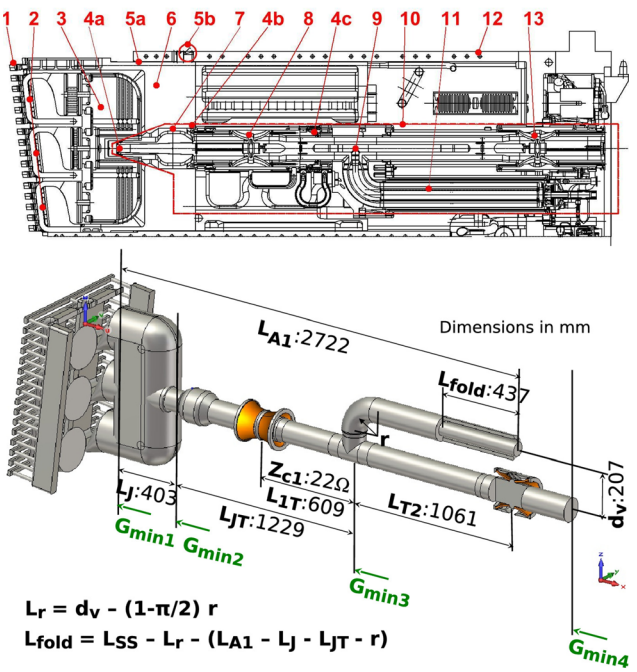

FIG. 1. (Upper) Section through of 1 of the 8 triplets of straps and their feeding RVTL: (1) Faraday Screen, (2) RF current straps, (3) 4PJ, (4) RVTL RF contacts (a and b) respectively, inner and outer conductors for assembly and shimming, (c) outer conductor for thermal expansion, (5) RF contacts (a) FHM-PP grounding for assembly and shimming, (b) deployable PP-VV grounding contact, (6) FHM, (7) direct line of sight neutron shield for 1st VCW, (8) front VCW, (9) SS-T, (10) RVTL, (11) SS, (12) PP, (13) rear VCW. (Lower) Schematic CST-MWS RF model layout showing the inner conductors of 1 of 8 similar triplets, 4PJ, VCWs (ceramics shown in orange), SS and RVTL assemblies with the parameters used for optimizing the performance.

plasma SOL profiles given by ITER Organization (IO)[9] depending on the physics assumptions used for modelling ITER's SOL. The "Low density SOL" case results in lower coupling than pre-project assumptions[10] while the "High density SOL" case is particularly favourable to couple ICRH power but may not be feasible due to the heat loads on ITER's First Wall (FW).

The S_{24}/Z_{24} matrix data are coupled to a RF circuit model of the circuit feeding the straps of which the components are represented by either S or Z matrices estimated with CST-MWS,[7] such as the 4 Port Junction (4PJ) feeding 3 poloidally adjacent straps, or simple Transmission Line (TL) sections for the rest of the Removable Vacuum Transmission Line (RVTL) which include the Service Stub tee (SS-T) and Vacuum Ceramic Windows (VCW). It was verified that the joining of the separate strap array matrix obtained from TOPICA to the S-matrix of the RF model of the 4PJ did not introduce errors due to the possible presence of non-TEM modes at the reference plane between the TOPICA strap array model and the 4PJ model.

The circuit components inside the port plug (PP) are optimized to maximize the power coupled to the plasma for the various phasings considered for operation taking into account geometrical constraints, assembly requirements and RF quantities specified by IO: E-field less than 2 kV/mm parallel to the magnetic field in the torus vacuum areas and magnitude less than 3 kV/mm everywhere and voltages less than 45 kV. Additionally, the CYCLE team has specified, subject to a successful outcome of related R&D,[11] currents less than 2 kA through RF contact with the highest current density (5 kA/m) between RVTL and 4PJ inner conductors. The arrows indicating the positions $G_{min,k}$ on Fig. 1 (lower) delimit the various sections where the circuit simulator verifies that the aforementioned electrical limits are not exceeded (formally $G_{min,k}$ refers to the minimum conductance and the power launched for 1 triplet is given by $P_{RF,k} = 0.5 \times G_{min,k} \times V^2_{max,k}$ for maximum voltage $V_{max,k}$ on an extended homogeneous TL longer than half wavelength feeding the respective section k,[10,12] where k = 1: antenna strap feeders, 2: 4PJ to the SS-tee, 3: SS-tee to the feeding MTL excluding 2nd VCW, 4: feeding MTL past the 2nd VCW). However, the circuit solver further takes into account (a) an estimate of the voltage distribution on the 4PJ, (b) that the maximum voltages do not always appear on the sections that are shorter than half a wavelength (allowing the transmitted power to increase if not limited elsewhere), (c) that the current density in the RF contact between 4PJ and RVTL inner conductor, I_{ct}, and (d) the electric field at the inward

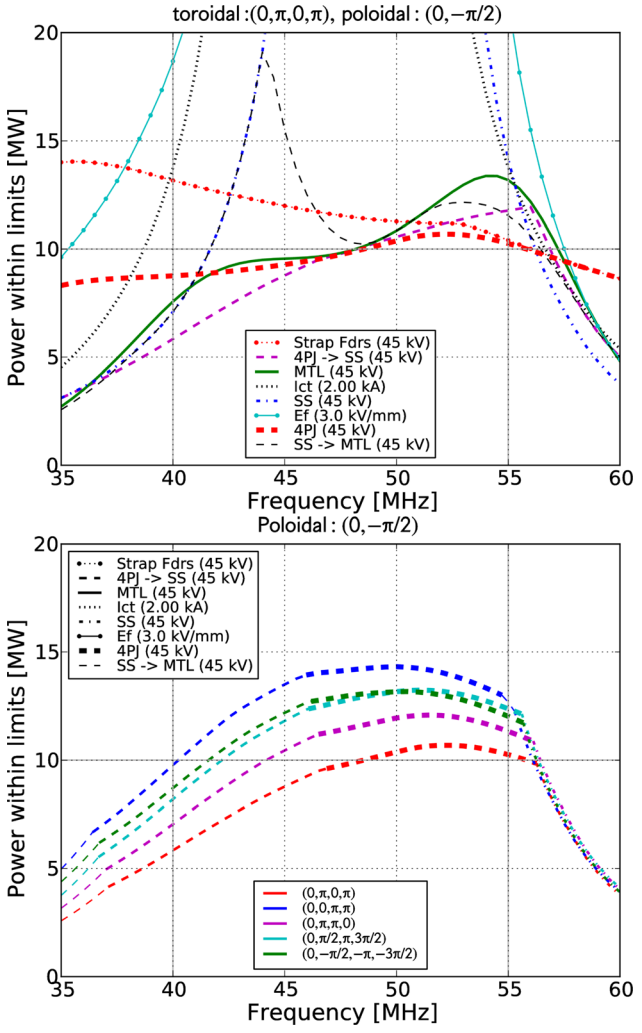

FIG. 2. (Upper) Estimated limits in coupled power for the allowable RF quantities in the various sections/locations of the strap feeding circuit (lower) resulting estimate of coupled power for the various toroidal phasings for the reference poloidal phasing (0, −π/2).

fold of the SS, E_f remain within allowed limits. Fig. 2 (upper) shows how the power coupled to the plasma is limited by the RF quantities in the various sections and locations for the toroidal phasing of (0, π, 0, π) and the reference poloidal phasing (0, $-\pi/2$). The resulting overall performance curve for this phasing is then the minimum over all curves and is shown in Fig. 2 (lower) together with similar curves for other toroidal phasings (the line style showing the nature of the limitation).

The maximum E-field on the components is limited by shaping their surface such that the design limits are not exceeded either at the maximum system voltage of 45 kV (4PJ, RVTL, VCW, SS) or at the maximum expected voltage (SS fold region): Fig. 3 (upper) shows the total and parallel (to B_T) electric fields on the 4PJ inner conductors.

The optimisation is most sensitive to the length of the 4PJ (L_J) for which an accuracy of $<$10 mm must be achieved: Fig. 3 (lower) illustrates that if the 4PJ is too long, the cliff-edge like limitation due to the RF contact current shifts downwards from the high frequency side and if it is too short the performance at the low frequencies is further degraded. For the other dimensional parameters, the sensitivity is not as severe.

The optimisation of the layout in terms of the parameters shown in Fig. 1 (lower) is not unique:[13] the solution presented in this paper uses two identical VCW assemblies with a slightly higher average characteristic impedance (to depart as little as possible of the optimal mechanical design of the VCW[14,15]) than that of the RVTL (20 Ω) at the cost of a slightly reduced performance at the high frequencies as well as reduction by about 0.3 MHz of the margin to the cliff-edge like limitations at high frequency.

The performance of the launcher is unsurprisingly very sensitive to the location of the SOL plasma profile in front of the antenna straps. Fig. 4 (upper) shows the power coupled to the plasma for profiles shifted (in an *ad hoc* manner in the input to the TOPICA coupling code) by 4 and 8 cm towards the antenna with respect to the reference position. It has been suggested by IO[16] that it should be possible to shift the plasma closer to the antenna while the heat load on the FW remains acceptable. Recently, a consistent plasma equilibrium has been received from IO[17] that amounts to a shift of the SOL profile towards the antenna by more than 10 cm. The compatibility with respect to the FW still needs to be assessed.

Finally, the performance can be improved by about 20% by feeding the array poloidally in (0, π) phasing rather than (0, $-\pi/2$) as shown in Fig. 4 (lower). Note that because the bottom triplets are installed upside down with respect to the top ones, feeding the array with (0, π) phasing poloidally actually means that the currents in the front face for the array are in phase poloidally (see Fig. 1 where the upper part

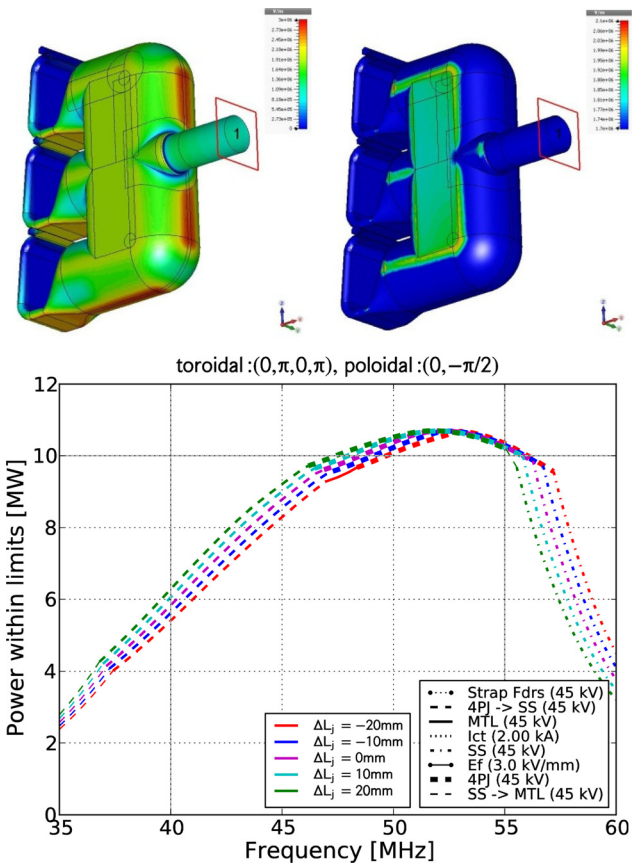

FIG. 3. (Upper) Electric fields on the 4PJ inner conductor at maximum voltage (53 MHz), color scale: E_{total} 0–3 kV/mm, $E_{\|}$ 1.7 − 2.1 kV/mm (2 kV/mm = yellow) (lower) sensitivity of the performance to the length dimension of the 4PJ (L_J).

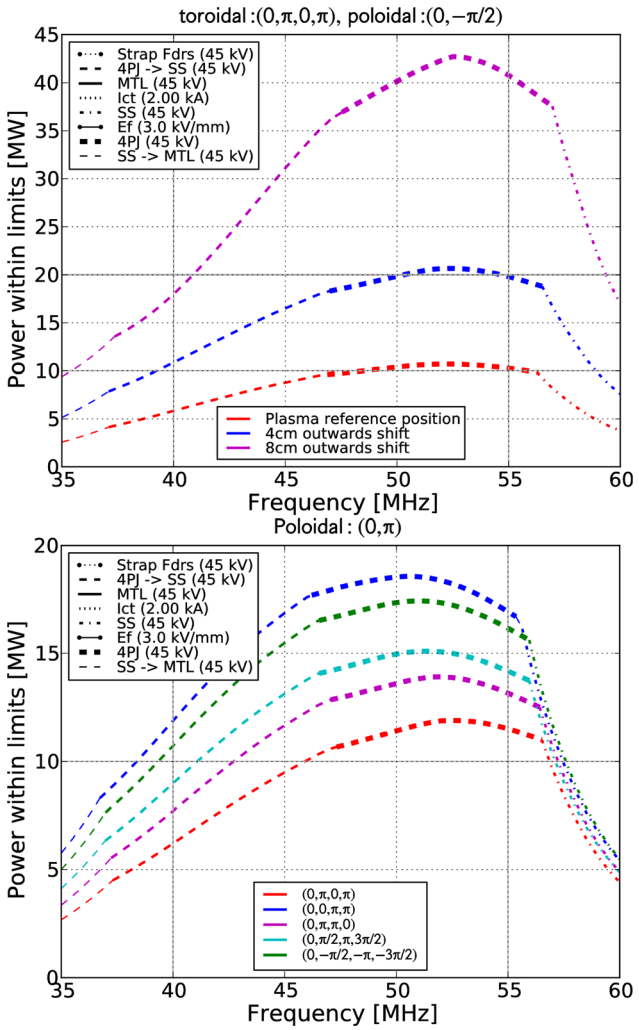

FIG. 4. (Upper) Performance for the (0, π, 0, π) toroidal phasing and (0, $-\pi/2$) poloidal phasing for SOL profiles shifted towards the antenna, (lower) coupled power for the various toroidal phasings for a poloidal phasing of (0, π).

shows a top triplet and the lower part shows a bottom triplet). A modification of the matching network to achieve this for toroidal current drive phasings has been proposed.[18] The effect of the poloidal phasing of the array on the power spectrum has been investigated with ANTITER II.[10] Fig. 5 shows the spectral resistance, $R_A(k_z)$ where $P_{RF} = \int \frac{1}{2} R_A(k_z) I_A{}^2 \, dk_z$ for an antenna current I_A and wave number k_z, for the positive current drive toroidal phasing for both poloidal phasings: for the waves launched in the region where surface waves could propagate this effect is modest and the overall excitation of this part of the spectrum appears to be slightly smaller for the $-\pi/2$ poloidal phasing. The gain of power launched at the spectral part of interest for the $(0, \pi)$ phasing is clear.

Losses are highest at high frequency with a minimum at mid-band frequency and amount to a maximum of 1.12 MW for the whole launcher at 55 MHz.[13]

III. RF MEASUREMENTS AND CONTROL ASPECTS

Redundant RF measurements are necessary to control the launched power spectrum, to operate the antenna within prescribed limits with confidence and to protect the launcher in case of arcs. Each RVTL asssembly is fitted with two pairs of RF probes that each measure local voltage and current simultaneously. Fig. 6 (upper, lower left) shows the location of the 4 probes on the RVTL outer conductor while Fig. 6 (lower right) shows that each probe is a little loop aligned to the axis of the RVTL and has 2 RF outputs, U_1 and U_2. Their (complex) sum reproduces a signal proportional to the local RF voltage and their difference one to the local RF current. These probes can also been used for Arc Detection although analysis shows that arcs located where the RF voltage of the Voltage Standing Wave (VSW) is low are not detected.[19] This a problem common to most arc detection techniques based on RF signals so that other methods should be used additionally.[20,21]

The estimates of performance shown assume that the control of the RF power feeding the strap array will be done using RF measurements of the amplitude and phase of the RF voltages located at the average position of the voltage anti-nodes on the 8 feeding main TLs.[10] As illustrated in Fig. 7, the main effect is that even with error free measurements

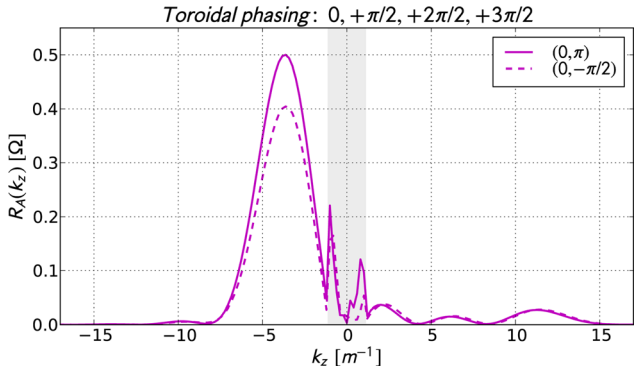

FIG. 5. Spectrum of the coupled power at 53 MHz ($k_0 = 1.11\,\mathrm{m}^{-1}$) for the positive current drive toroidal phasing. The shaded area shows the part of the spectrum where $k_z < k_0$. The plain lines are for the $(0, \pi)$ poloidal phasing and the dashed lines are for the $(0, -\pi/2)$ one.

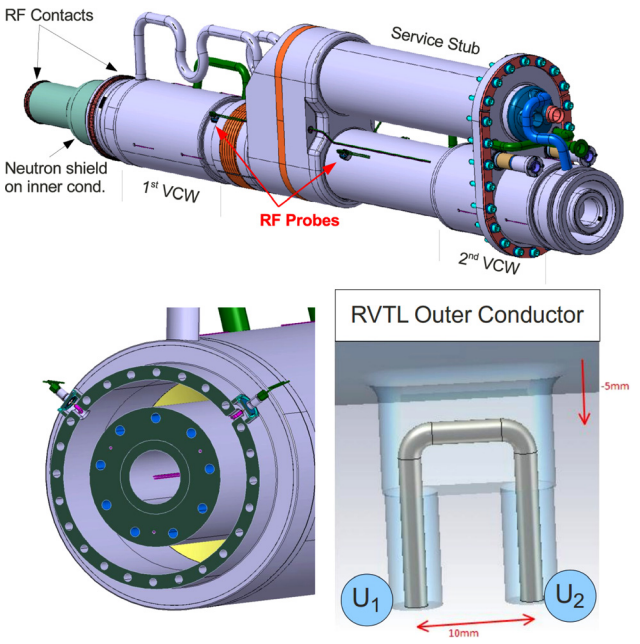

FIG. 6. (Upper) location of RF probes on the RVTL (lower left) pairs of probes at the same location on the RVTL (lower right) details of RF probes.

the errors on the strap current amplitude and phases will be substantially larger than for the ideal (but possibly not feasible) control which mathematically minimizes the strap current amplitude and phase errors.[22] Note that because there are 24 straps and only 8 feeding TLs and the presence of asymmetries due to, e.g., the non-reciprocity of the plasma, the strap current amplitude and phase errors cannot be zeroed even in the case of an ideal control. These errors become larger when the coupling with the plasma is increased and when the phasing (poloidal as well as toroidal) leads to RF power transfers ($\pi/2$ phase differences between adjacent triplets). These amplitude and phase errors may in turn increase RF sheath losses on the Antenna's Faraday Screen (FS) and adjacent Blanket Shielding Modules (BSM). Although progress has been made in the modelling of the physics of RF sheath in tokamak environments,[23,24] the problem remains computationally complex, still necessitating geometric as well as physics simplifications such that a sufficiently accurate quantification of the RF power dissipated in the RF sheaths is still outstanding. In order to cope with these uncertainties, the position of the launcher with respect to the plasma can be varied during shutdowns: it can be moved 1 cm towards the plasma to improve the coupling should it be too marginal and 2 cm away from the plasma should RF sheaths and other heat loads on the FS bars exceed their thermal capabilities.

IV. GROUNDING AND RF EXCITATION OF BSM STRUCTURES

Theoretical and experimental[25,26] efforts were spent to understand the aspects of the grounding of the PP to the Vacuum Vessel (VV) to avoid spurious resonances in the 24x24 strap impedance matrix[27] as well as the presence of high electric fields in the nominal 20 mm gap between the PP and VV[28] as well as to experimentally validate the proposed

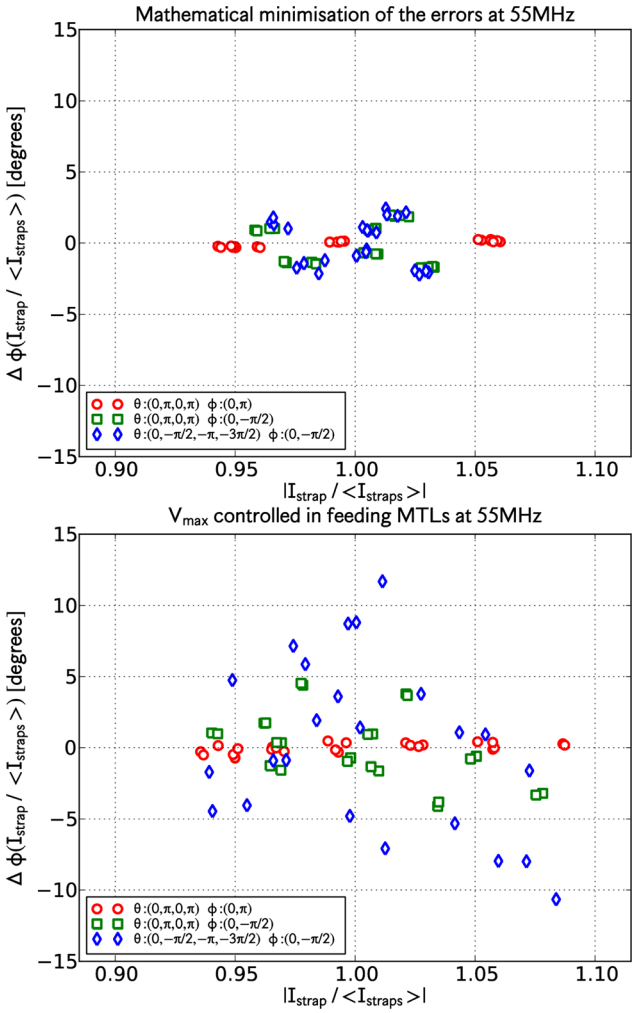

FIG. 7. Amplitude and phase errors with respect to an ideal distribution of RF current on the 24 straps of the array for the various toroidal phasings (θ) and poloidal phasings (ϕ) (upper) using a theoretical Least Square Fit on the 8 complex forward power waves feeding the array (lower) using amplitude and phase control of the 8 RF voltages at the average location of the voltage anti-node in the feeding MTLs.

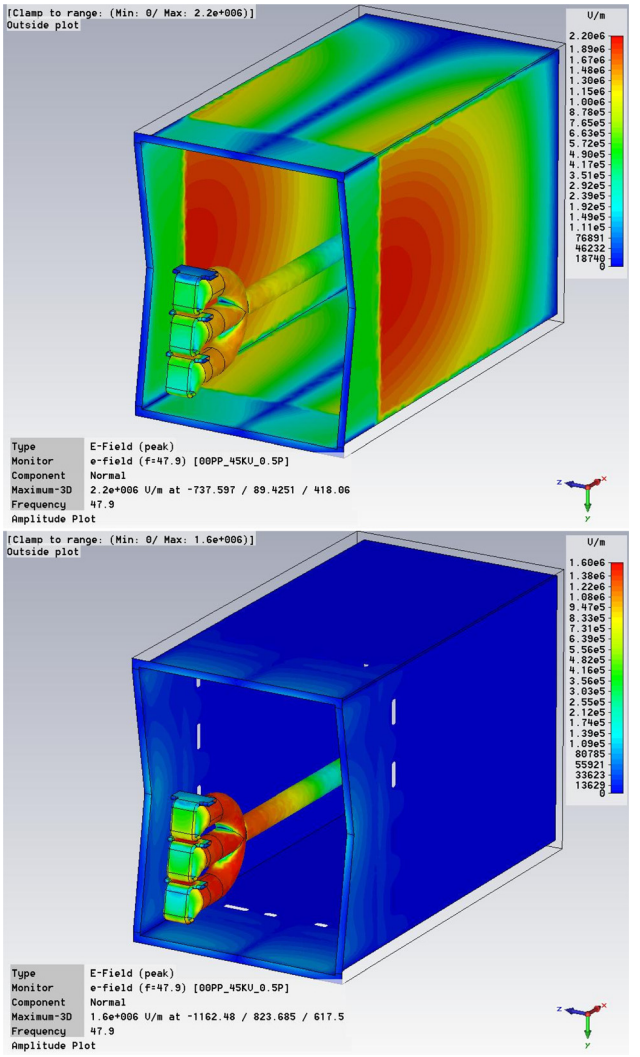

FIG. 8. (Upper) E-fields between the PP and VV when the PP is only grounded by the main port flange. For comparison one of 8 triplets fed from a simplified 4PJ is shown with the electric fields at system voltage of 45 kV at 47.9 MHz with a $00\pi\pi$ toroidal and 0π poloidal excitation. (Lower) The electric fields for the same excitation but with the proposed grounding located at approx. 1 m from the front of the launcher using discrete flexible contact strips between PP and VV.

grounding solution between the VV-BSM structure and the PP.

Fig. 8 shows the effectiveness of the proposed grounding to reduce electric fields in these areas: without the additional grounding towards the front of the PP the fields can even exceed these on the high power components of the launcher.[29]

The possible appearance of resonances on the coupled power vs. frequency curves is due to the presence of gaps of varying widths between the front of the launcher and the surrounding BSM.[27] Fig. 9 (upper) shows the effect of the absence of adequate grounding on the power coupled vs. frequency curves. Fig. 9 (lower) identifies the various resonances appearing in the case of the toroidal monopole phasing and clearly shows that these resonances are adequately suppressed by the proposed grounding.[25] It is expected that these resonances, which are quite narrow, when appearing at or near the operating frequency are affecting the launched power spectrum while if the resonance is further away the power spectrum will not be affected significantly. However, at present, there are no tools available to analyse this in a detailed quantitative manner.

In ITER, the blanket modules covering the first wall, whose dimensions are of the order of the ICRF wavelengths, together with the clearance gaps between them constitute a corrugated wall structure which will interact with the electromagnetic waves launched by the ICRF antennas. The conditions in which the grooves constituted by the clearance gaps between two neighbouring blanket modules can become resonant, i.e., present infinite input impedance, are being studied using two approximate analytical models: a groove shorted at both ends (shorted rectangular waveguide) and a groove closed on itself (shorted coaxial waveguide). The waveguide excitation is provoked by the tangential RF magnetic field produced by the antenna array on its surrounding wall. The amount of excitation depends on the way this excitation matches the field distribution of the waveguide mode at its aperture. In case of resonant conditions, a mode can be

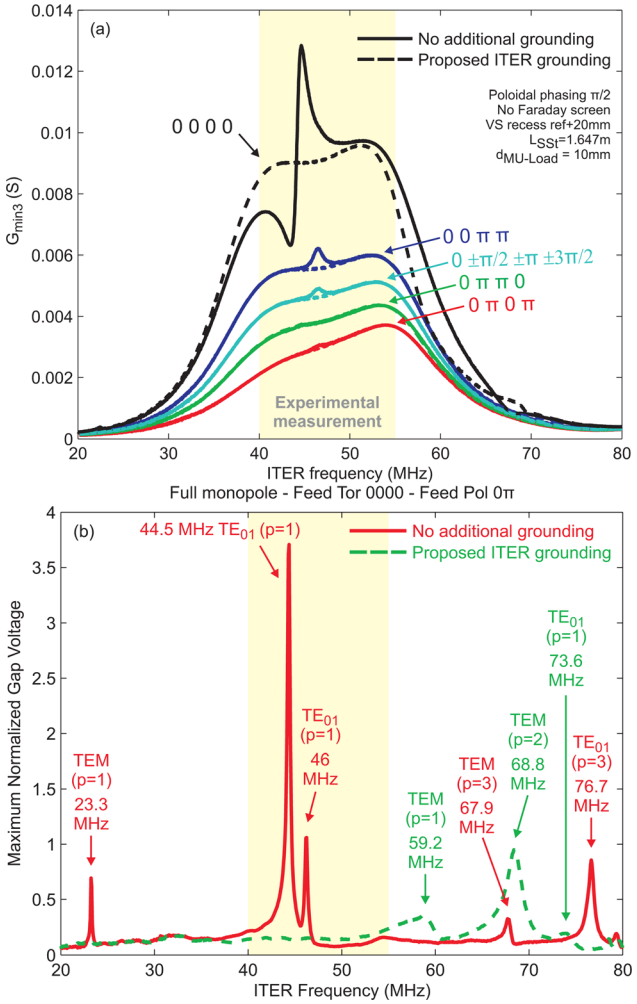

FIG. 9. (Upper) Experimental measurement on the low power mock-up of the effect of the (absence of) adequate grounding on the power coupled vs. frequency for the various toroidal phasings. (Lower) The gap voltage vs. frequency normalized to average strap voltages for the toroidal monopole phasing (0, 0, 0, 0) and (0, π) poloidal phasing with and without grounding identifying the various types of resonance modes.

excited in the shorted waveguide potentially leading to large electric field between the waveguide walls and coupling to the antenna excitation. A similar approach was used analyzing the effect of the clearance gap around the antenna and led to the definition[28] and test[25] of a grounding solution for the ITER ICRF antenna as well as the analysis of a resonance appearing in the ITER frequency band in the modelling when using simplified blanket geometry around the antenna.[27] The analysis is performed here for gaps around blanket modules. We finally examine the effect of the first wall structure, which is acting as a spatially periodic (toroidally and poloidally) corrugated structure, on the wave propagation along it.

A. Shorted rectangular waveguide

The groove constituted by the clearance gap between two neighboring blanket modules is first approximated by a lossless rectangular waveguide. The geometry of such a waveguide is shown in Fig. 10(a), where a is the blanket module's length and b is the width of the clearance gap, with

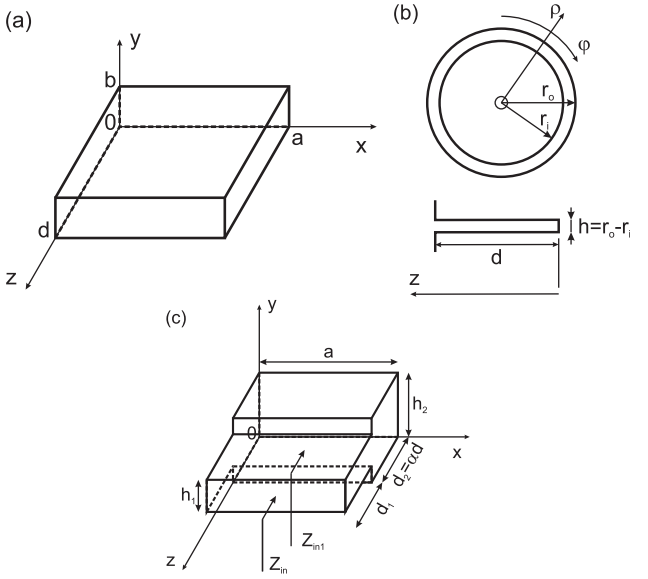

FIG. 10. Geometry of the waveguides (a) rectangular (b) circular coaxial (c) rectangular of the mushroom type.

typically $b \ll a$. The waveguide has a length d, being shorted at the back at the vessel wall ($z=0$) and opened at the front by the clearance gap ($z=d$). The boundary conditions are that the tangential electric field components are zero on the walls of the waveguide, meaning $E_x=0$ at $y=0$, b, $E_y=0$ at $x=0$, a and $E_x=E_y=0$ at $z=0$. The derivative of the tangential electric field is in first approximation taken as zero at the mouth of the waveguide, i.e., at $z=d$. TE and TM modes can be excited in a rectangular waveguide. The resonance frequencies of these modes can be found in the same way as the ones of a resonant cavity[30] replacing the short circuit boundary condition by an open circuit boundary condition at $z=d$. Cutoff frequencies for the TE_{mn} and TM_{mn} modes and resonance frequencies for the TE_{mnp} and TM_{mnp} where $\beta d = p\pi/2$, $p=1, 3, 5,\ldots$ are then given by

$$f_{c,mn} = \frac{c}{2\pi}\sqrt{\left(\frac{m\pi}{a}\right)^2+\left(\frac{n\pi}{b}\right)^2}$$
$$f_{res,mnp} = \frac{c}{2\pi}\sqrt{\left(\frac{m\pi}{a}\right)^2+\left(\frac{n\pi}{b}\right)^2+\left(\frac{p\pi}{2d}\right)^2}$$
$$m,n = 0,1,2,\ldots; \quad p = 1,3,5,\ldots \tag{1}$$

The TE_{10} mode has the lowest cutoff and is the dominant mode. TM_{11} is the first TM mode. As $b \ll a$, the TM modes typically have cutoff frequencies in the GHz range and hence will not be excited in the ICRF frequency band. The dominant resonant mode is the TE_{101} mode, corresponding to the TE_{10} dominant waveguide mode in a guide of length $\lambda_g/4 = 2\pi/\beta_{10}$, where β_{10} is the propagation constant of the dominant mode. Its cutoff frequency (only dependent on a), corresponding cutoff wavelength and propagation constant are given by

$$f_c = \frac{c}{2a}, \quad \lambda_c = 2a, \quad \beta = k_0\sqrt{1-\left(\frac{f_c}{f}\right)^2}, \tag{2}$$

where $k_0 = 2\pi f/c$. The field components and wave impedance are given by (forward and backward waves):

$$E_y = \left(E_+ e^{-j\beta z} + E_- e^{j\beta z}\right)\sin\frac{\pi x}{a} = E_0 \sin\frac{\pi x}{a}\sin\frac{p\pi z}{2d}$$
$$H_x = -j\frac{E_0}{Z_{TE}}\sin\frac{\pi x}{a}\sin\frac{p\pi z}{2d}, \quad Z_{TE} = \eta\frac{4d}{p\lambda} \tag{3}$$

where $\eta = \sqrt{\mu_0/\epsilon_0} \approx 377\Omega$ is the vacuum intrinsic impedance and $E_0 = V_{gap}/b$, where $V_{gap} = V$ $(x = a/2, z = d)$.

B. Shorted coaxial waveguide

The clearance gap all around a blanket module can be approximated by a shorted circular coaxial waveguide of equivalent inner radius r_i and outer radius r_o with $h = r_o - r_i \ll r_i$, shorted at $z = 0$ and open at $z = d$ (Fig. 10(b)). A particular case was already treated in the case of the clearance gap surrounding the ITER antenna,[27,28] for which an adequate grounding solution was proposed and experimentally validated on a reduced-scale mock-up.[25] In the case of a coaxial structure, *TEM* modes, in addition to *TE* and *TM* modes, can be excited. The dominant modes are the *TEM*, which has no cutoff, and the TE_{10} modes. Equations (1) and (2) expressing the cutoff and resonance frequencies, the cutoff wavelength and propagation constant remain valid with $m, n = 0, 1, 2, 3, \ldots$ for TE_{mnp} and TM_{mnp} modes, $m, n = 0$ for TEM_p modes and $p = 1, 3, 5 \ldots$ provided the following replacements are performed: $a/\pi \rightarrow a_{eq} = (r_o + r_i)/2$ and $b \rightarrow h = r_o - r_i$ with $h \ll r_i$.[31] Expressions for the fields for the coaxial waveguide are given in Refs. 28 and 31.

C. Mushroom type waveguides

Let us now consider a *mushroom*-type rectangular waveguide, i.e., a rectangular waveguide presenting a height transition as shown in Fig. 10(c) (section cut). The waveguide has a total depth $d = d_1 + d_2$ and let us define $d_2 = \alpha d$ and $d_1 = (1-\alpha)d$ with $0 < \alpha < 1$. The height is changing from $b = h_1$ to $b = h_2$ and the height ratio is given by $\kappa = h_2/h_1$. The input impedance seen from region 1 looking towards region 2 is the one of a shorted transmission line of characteristic impedance Z_{02} and with a propagation constant β, i.e.,

$$Z_{in1} = jZ_{02}\ \tan[\beta d_2] = jZ_{02}\ \tan(\beta\alpha d)$$
$$Z_{02} = \frac{V}{I} = \frac{\pi}{2}\frac{h_2}{a}\frac{E_y}{H_x} = \frac{\pi}{2}\frac{h_2}{a}Z_{TE}, \tag{4}$$

where Z_{02} is the rectangular waveguide's characteristic impedance based on the maximum V.[32] In this case, we also have $\kappa = h_2/h_1 = Z_{02}/Z_{01}$ as the wave impedance Z_{TE} is independent of the waveguide geometry. The input impedance seen looking towards the rectangular mushroom-type shorted waveguide is

$$Z_{in} = Z_{01}\frac{Z_{in1} + jZ_{01}\tan(\beta(1-\alpha)d)}{Z_{01} - jZ_{in1}\tan(\beta(1-\alpha)d)} = jZ_{01}\frac{\kappa\ \tan[\beta\alpha d] + \tan(\beta(1-\alpha)d)}{1 - \kappa\ \tan[\beta\alpha d]\tan(\beta(1-\alpha)d)}. \tag{5}$$

The waveguide is resonant for the frequencies for which $Z_{in} \rightarrow \infty$. An example of resonant frequencies (for $p = 1$) in function of α for different values of κ is given in Fig. 11 (top) for a waveguide with typical values for ITER: $a = 1$ m, $b = 0.02$ m, and $d = 0.4$ m. Excellent agreement is found between the values from the analytical model and those from a numerical eigenmode solver.

Experimental gap voltage measurement at the aperture of a rectangular shorted mushroom waveguide placed on the first wall of the ITER ICRF reduced-scale antenna mock-up[25] further supports the result (see Fig. 11 (bottom), monopole phasing case): resonance frequencies are decreasing when κ is increasing for given α and d. Resonances are measured around 222 MHz for $\kappa = 54$ and 275 MHz for $\kappa = 17$ on the mock-up (model predicts, respectively, 212 MHz and 295 MHz). For a given operation frequency, there is no resonance if $\kappa < \kappa_{min} = 1/\tan^2(\beta d/2)$, a single value of α leading to resonance for $\kappa = \kappa_{min}(\alpha = 0.5)$ and 2 values of a leading to resonance for $\kappa > \kappa_{min}$. The same procedure can be applied to study the effect of a mushroom-type circular coaxial waveguide. Equation (5) remains valid in first approximation (for $a_{eq} \gg h$, $\kappa = [a_{eq1}h_2]/[a_{eq2}h_1] \approx h_2/h_1$). The resonance frequencies in function of α and κ for the *TEM* for a coaxial waveguide with $a_{eq} = 4 \times 1/2\pi = 0.64$ m, $h = 0.02$ m and $d = 0.4$ m is shown in Fig. 11 (middle). In this case, $\beta = k_0$ and the result is independent of a_{eq}. One can see that the resonant frequency can substantially decrease, potentially towards the operation frequency range (40–55 MHz in the case of ITER), when the waveguide exhibits a transition towards a larger height waveguide. The resonant frequency for a constant height waveguide ($\kappa = 1$) is in agreement with the value given by Eq. (1). No resonance effect is expected for a constant width groove of length $d = 0.4$ m in the ITER ICRF frequency range.

D. Effect of a corrugated wall structure

A corrugated wall acts as a slow wave structure[31] ($v_{phase} < c$) with spatial period L Fig. 12 (left). The propagation constant linked with the fundamental wave (higher order Fourier components are linked with its spatial harmonics) can be derived by matching the average value of the surface impedance of the corrugated wall, which is different from zero (as it would be for a flat metallic wall), $\langle Z_s \rangle = -j\eta h/L\ \tan(k_0 d)$, to the surface wave impedance $Z_{s,w} = -E_y/H_z$. In the case of high density plasma facing a corrugated wall and $k_z = 0$ (or $\partial\partial/\partial z = 0$) one can show that we have

$$\langle Z_s \rangle = -j\frac{\omega\mu_0}{k_0}\frac{h}{L}\ \tan(k_0 d) = -j\omega\mu_0\frac{\sqrt{\beta_0{}^2 - k_0{}^2}\ \tanh\left(a\sqrt{\beta_0{}^2 - k_0{}^2}\right)}{k_0{}^2} = Z_{s,w}. \tag{6}$$

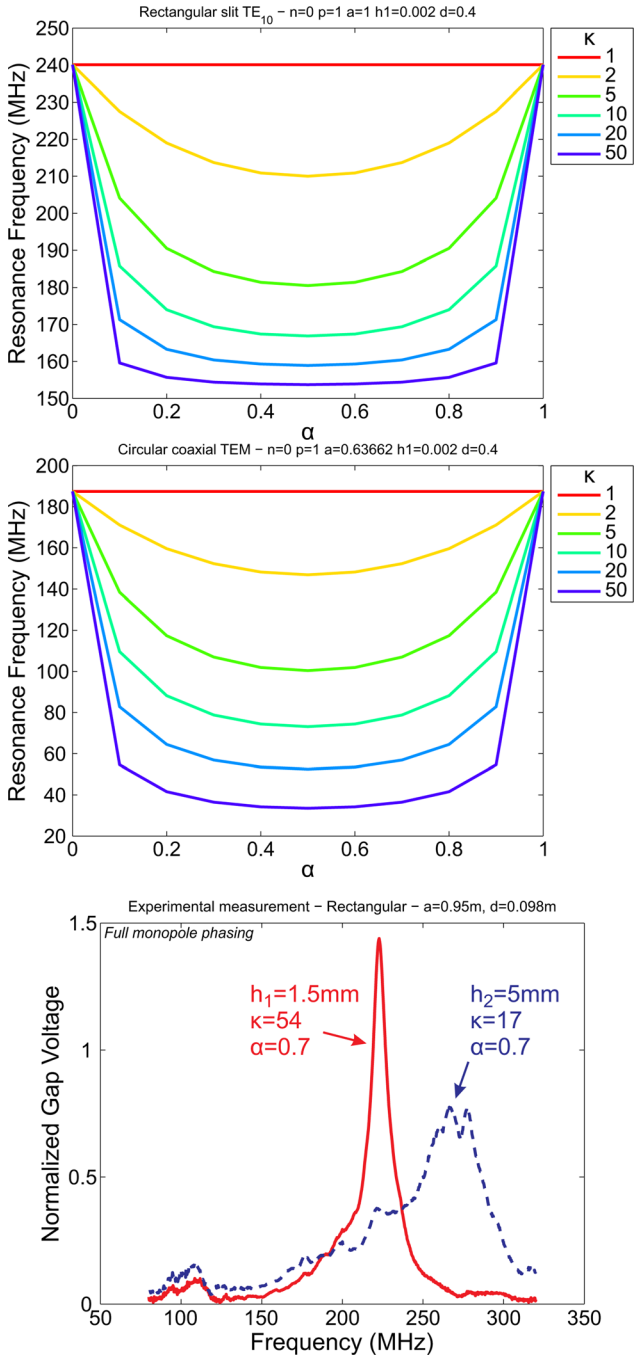

FIG. 11. Resonant frequencies in function of α (depth ratio) and κ (height ratio) for (top) the TE_{101} mode in a rectangular mushroom type waveguide with $a = 1$ m, $h_1 = 0.02$ m and $d = 0.4$ m (middle) the TEM_1 mode in a mushroom type circular coaxial waveguide with $a_{eq1} = 4 \times 1/2\pi = 0.64$ m, $h_1 = 0.02$ m and $d = 0.4$ m. (Bottom) Experimental measurement of gap voltage normalized to strap voltages on ITER ICRF antenna reduced-scale mock-up; resonances of the rectangular mushroom type shorted waveguide ($a = 0.95$ m, $h_1 = 1.5$ or 5 mm, $h_2 = 79.8$ mm $+ h_1$, $d_1 = 29.9$ mm, $d_2 = 68.8$ mm) occur around 222 MHz and 275 MHz.

An example of the effect of the distance to the plasma a and of the groove width h on the propagation constant is given in Fig. 12 (right) for an ITER-relevant case with f = 55 MHz, L = 1 m, and d = 0.4 m (high density plasma approximation). The coaxial modes dispersion is consequently extended towards a larger k_y, k_z domain ($|k_{y,z}| < \beta_0$ instead of $|k_{y,z}| < k_0$). For a doubly corrugated wall, the

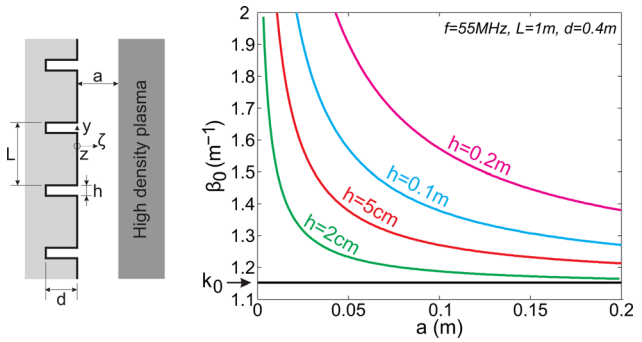

FIG. 12. Corrugated wall structure (left) geometry (right) effect on the propagation constant.

toroidal and poloidal grooves have a wave surface impedance $Z_{s,w,tor} = -(E_y/H_z)_{tor}$ and $Z_{s,w,pol} = -(E_z/H_y)_{pol}$ excited, respectively, by the H_z and H_y radiated field components. The antenna exciting mainly a TE/z field the poloidal grooves will be less excited but can produce a coupling between TE/z and TM/z waves.

However, it is stretching present day computational capabilities to model the RF fields surrounding the real geometry of the objects and gaps in the vicinity of the front of the antenna such as cooling pipes ELM stabilization coils with their detailed grounding and attachments to the VV in order to exclude the presence of similar resonances appearing in the frequency band of interest. The CYCLE team has proposed to develop and test on scaled mock-ups of the launcher[12] low power measurement procedures on the installed port plug to detect possible resonances and avoid operating at these frequencies if detected.

V. CONCLUSIONS

The proposed layout for the ITER ICRF launcher has been optimized to maximize the coupled power on the worst case plasma SOL profile provided by IO. It is expected that at least 10 MW/launcher can be coupled to the plasma at frequencies above the mid-band frequency for all toroidal phasings and a poloidal phasing of $(0, -\pi/2)$. The location of the plasma SOL is a very sensitive parameter and it is very likely that the situation can be improved substantially. The sensitivity of the optimisation to the dimensional parameters appears to be mechanically reasonable and on the order of about 10 mm for the most sensitive component.

Particular attention has been given to the RF grounding aspects of the launcher to avoid spurious resonances and high electric fields in the gap between the PP and the VV port. Simple analytical models allow analyzing the possible wave perturbation in the ICRF operating band by the grooves between the blanket modules. Conditions for resonance are given and it is shown that no resonance is expected in the case of constant-width grooves of sufficiently small length as is the case in ITER. Mushroom-type structures (larger gap at the shorted side) however can bring down the resonance frequencies and one should take care to avoid bringing them in the ICRF operation domain. The wall corrugation grating acts as a slow wave structure which could modify the wall boundary condition and hence the wave propagation along it.

This perturbation should remain negligible if the groove width stays constant along its depth but otherwise could modify the coaxial modes dispersion and extend it in a larger k_y, k_z domain. It is consequently advised to avoid as much as possible mushroom-shaped blanket modules and avoid antenna array phasing with significant low k_z (i.e., ($|k_z| \leq k_0$) excitation.

ACKNOWLEDGMENTS

The project F4E-2009-GRT-026 has been funded with support from Fusion for Energy (F4E). This publication reflects the views only of the authors, and F4E cannot be held responsible for any use which may be made of the information contained herein. The views and opinions expressed do not necessarily reflect those of the ITER Organization.

[1]P. Lamalle, B. Beaumont, F. Kazarian, T. Gassmann, G. Agarici, P. Ajesh, T. Alonzo, B. Arambhadiya, A. Argouarch, R. Bamber, G. Berger-By, J. M. Bernard, C. Brun, S. Carpentier, F. Clairet, L. Colas, X. Courtois, A. Davis, C. Dechelle, L. Doceul, P. Dumortier, F. Durodié, F. Ferlay, M. Firdaouss, E. Fredd, J. C. Giacalone, R. Goulding, N. Greenough, D. Grine, D. Hancock, J. V. S. Hari, J. Hillairet, J. Hosea, S. Huygen, J. Jacquinot, J. Jacquot, A. S. Kaye, D. Keller, V. Kyrytsya, D. Lockley, F. Louche, H. Machchhar, E. Manon, N. Mantel, R. Martin, M. McCarthy, A. Messiaen, L. Meunier, D. Milanesio, M. Missirlian, K. Mohan, A. Mukherjee, M. Nightingale, D. Patadia, A. M. Patel, G. Perrollaz, B. Peters, R. Pitts, M. Porton, K. Rajnish, D. Rasmussen, D. Rathi, R. Sanabria, R. Sartori, M. Shannon, A. Simonetto, R. Singh, G. Suthar, D. Swain, P. Thomas, P. Tigwell, R. G. Trivedi, M. Vervier, M. Vrancken, D. Wilson, and K. Winkler, "Status of the ITER Ion Cyclotron H&CD system," Fusion Eng. Des. **88**, 517–520 (2013); in proceedings of the 27th Symposium On Fusion Technology (SOFT-27), edited by O. Neubauer, R. Koch, P. Mertens, and T. Verhoeven, Liège, Belgium, 24–28 September 2012.

[2]F. Durodié, M. P. S. Nightingale, M. L. Mayoral, J. Ongena, A. Argouarch, G. BergerBy, T. Blackman, V. Cocilovo, A. Czarnecka, S. Dowson, D. Frigione, R. Goulding, M. Graham, J. Hobirk, S. Huygen, S. Jachmich, P. Jacquet, E. Lerche, P. U. Lamalle, T. Loarer, R. Maggiora, A. Messiaen, D. Milanesio, I. Monakhov, M. F. F. Nave, F. Rimini, H. Sheikh, C. Sozzi, M. Tsalas, D. Van Eester, M. Vrancken, A. Whitehurst, E. Wooldridge, K. D. Zastrow, and JET-EFDA Contributors, "Physics and engineering results obtained with the ion cyclotron range of frequencies ITER-like antenna on JET," Plasma Phys. Controlled Fusion **54**, 074012 (2012).

[3]V. Lancellotti, D. Milanesio, R. Maggiora, G. Vecchi, and V. Kyrytsya, "Topica: An accurate and efficient numerical tool for analysis and design of ICRF antennas," Nucl. Fusion **46**, S476 (2006).

[4]D. Milanesio, O. Meneghini, V. Lancellotti, R. Maggiora, and G. Vecchi, "A multi-cavity approach for enhanced efficiency in topica rf antenna code," Nucl. Fusion **49**, 115019 (2009).

[5]M. Graham, M. L. Mayoral, I. Monakhov, J. Ongena, T. Blackman, M. P. S. Nightingale, E. Wooldridge, F. Durodié, A. Argouarch, G. Berger-By, A. Czarnecka, S. Dowson, R. Goulding, S. Huygen, P. Jacquet, T. J. Wade, E. Lerche, P. U. Lamalle, H. Sheikh, D. Van Eester, M. Vrancken, A. Walden, A. Whitehurst, and JET-EFDA Contributors, "Implementation of load resilient ion cyclotron resonant frequency (ICRF) systems to couple high levels of ICRF power to ELMy H-mode plasmas in JET," Plasma Phys. Controlled Fusion **54**, 074011 (2012).

[6]I. Monakhov, M. Graham, T. Blackman, S. Dowson, F. Durodié, P. Jacquet, J. Lehmann, M. L. Mayoral, M. P. S. Nightingale, C. Noble, H. Sheikh, M. Vrancken, A. Walden, A. Whitehurst, E. Wooldridge, and J.-E. Contributors, "Design and operations of a load-tolerant external conjugate-T matching system for the A2 ICRH antennas at JET," Nucl. Fusion **53**, 083013 (2013).

[7]*CST Microwave Studio®, User Manual* (CST GmbH, 2011).

[8]A. Messiaen and R. Weynants, "ICRH antenna coupling physics and optimum plasma edge density profile. Application to ITER," Plasma Phys. Controlled Fusion **53**, 085020 (2011).

[9]S. Carpentier, R. Pitts, P. Stangeby, J. Elder, A. Kukushkin, S. Lisgo, W. Fundamenski, and D. Moulton, "Modelling of beryllium erosion-redeposition on {ITER} first wall panels," J. Nucl. Mater. **415**, S165–S169 (2011); in Proceedings of the 19th International Conference on Plasma-Surface Interactions in Controlled Fusion.

[10]A. Messiaen, R. Koch, R. R. Weynants, P. Dumortier, F. Louche, R. Maggiora, and D. Milanesio, "Performance of the ITER ICRH system as expected from TOPICA and ANTITER II modelling," Nucl. Fusion **50**, 025026 (2010).

[11]A. Argouarch, R. Bamber, J. M. Bernard, J. M. Delaplanche, F. Durodié, S. Larroque, P. Lecomte, G. Lombard, J. C. Hatchressian, P. Mollard, D. Mouyon, M. Pagano, J. C. Patterlini, S. Rasio, B. Soler, L. Toulouse, D. Thouvenin, J. M. Verger, T. Vigne, and R. Volpe, "Steady state RF facility for testing ITER ICRH RF contact component," Fusion Eng. Des. **88**, 1002–1006 (2013); in Proceedings of the 27th Symposium On Fusion Technology (SOFT-27), edited by O. Neubauer, R. Koch, P. Mertens, and T. Verhoeven, Liège, Belgium, 24–28 September 2012.

[12]P. Dumortier, F. Durodié, D. Grine, V. Kyrytsya, F. Louche, A. Messiaen, M. Vervier, and M. Vrancken, "Validation of the rf properties and control of the iter icrf antenna," in *Proceedings Fusion Energy 2012* (2012), Vol. IAEA-CN-197, pp. ITR/P1–07; presented at the 24th IAEA Fusion Energy Conference, 8–13 October 2012, San Diego, CA, USA.

[13]M. Vrancken, F. Durodié, R. Bamber, N. Dalton, P. Dumortier, M. Graham, A. Horvat, D. Hancock, D. Lockley, F. Louche, R. Maggiora, A. Messiaen, D. Milanesio, M. P. S. Nightingale, M. Shannon, P. Tigwell, M. Van Schoor, D. Wilson, K. Winkler, and C. Team, "RF optimisation of the port plug layout and performance assessment of the ITER ICRF antenna," Fusion Eng. Des. **88**, 940–944 (2013); in Proceedings of the 27th Symposium On Fusion Technology (SOFT-27), edited by O. Neubauer, R. Koch, P. Mertens, and T. Verhoeven, Liège, Belgium, 24–28 September 2012.

[14]C. Hamlyn-Harris, A. Borthwick, J. Fanthome, C. Waldon, M. Nightingale, and N. Richardson, "Engineering design of an {RF} vacuum window for the {ITER} {ICRH} antenna," Fusion Eng. Des. **84**, 887–894 (2009); in Proceeding of the 25th Symposium on Fusion Technology (SOFT-25).

[15]R. C. Walton and A. Kaye, "A continuous wave RF vacuum window," JET Report JET-R(99)03, 1999.

[16]A. Loarte, private communication (2010).

[17]S. Carpentier, R. A. Pitts, P. C. Stangeby, J. D. Elder, A. S. Kukushkin, S. Lisgo, W. Fundamenski, and D. Moulton, J. Nucl. Mater. **415**, S165–S169 (2011).

[18]M. Vervier, A. Messiaen, and P. Dumortier, "Technical optimization of the ITER ICRH decoupling and matching system," Fusion Eng. Des. **88**, 1030–1033 (2013); in Proceedings of the 27th Symposium On Fusion Technology (SOFT-27), edited by O. Neubauer, R. Koch, P. Mertens, and T. Verhoeven, Liège, Belgium, 24–28 September 2012.

[19]S. Huygen, P. Dumortier, F. Durodié, A. Messiaen, M. Vervier, M. Vrancken, E. Wooldridge, and the CYCLE Team, "Proposal of an arc detection technique based on rf measurements for the iter icrf antenna," AIP Conf. Proc. **1406**, 21–24 (2011); Proceedings of the 19th Topical Conference on Radio Frequency Power in Plasmas, Newport (USA), 1–3 June 2011.

[20]R. D'Inca, "Arc detection for the ICRF system on ITER," AIP Conf. Proc. **1406**, 5–12 (2011).

[21]S. M. Salvador, R. Maggiora, R. D'Inca, and H. Fuenfgelder, "Arc detection with GUIDAR: First experimental tests on MXP testbed," AIP Conf. Proc. **1406**, 25–28 (2011).

[22]M. Vrancken, F. Durodié, P. Dumortier, D. Lockley, F. Louche, A. Messiaen, R. Maggiora, D. Milanesio, M. P. S. Nightingale, P. Tigwell, M. Van Schoor, D. Wilson, and the CYCLE Team, "Optimization of the layout of the ITER ICRF antenna port plug and its performance assessment," AIP Conf. Proc. **1406**, 61–64 (2011); in Proceedings of the 19th Topical Conference on Radio Frequency Power in Plasmas, Newport (USA) 1–3 June 2011.

[23]L. Colas, J. Jacquot, S. Heuraux, E. Faudot, K. Crombé, V. Kyrytsya, J. Hillairet, and M. Goniche, "Self consistent radio-frequency wave propagation and peripheral direct current plasma biasing: Simplified three dimensional non-linear treatment in the 'wide sheath' asymptotic regime," Phys. Plasmas **19**, 092505 (2012).

[24]J. Jacquot, D. Milanesio, L. Colas, S. Heuraux, and M. Goniche, "Recent advances in self-consistent RF sheath modeling and related physical properties: Application to Tore Supra IC antennae," in 39th EPS Conference and 16th International Congress on Plasma Physics (2012), see http://ocs.ciemat.es/EPSICPP2012PAP/pdf/P2.038.pdf.

[25]P. Dumortier, V. Kyrytsya, F. Louche, A. Messiaen, M. Vervier, and F. Durodié, "ITER ICRH antenna grounding options," Fusion Eng. Des. **88**, 922–925 (2013); in Proceedings of the 27th Symposium on Fusion Technology (SOFT-27), edited by O. Neubauer, R. Koch, P. Mertens, and T. Verhoeven, Liège, Belgium, 24–28 September 2012.
[26]D. Hancock, M. Shannon, B. Beaumont, P. Dumortier, F. Durodié, V. Kyrytsya, F. Louche, R. McKinley, and K. Nicholls, "Design of a mechanically actuated RF grounding system for the ITER ICRH antenna," Fusion Eng. Des. **88**, 2100–2104 (2013); in Proceedings of the 27th Symposium on Fusion Technology (SOFT-27), edited by O. Neubauer, R. Koch, P. Mertens, and T. Verhoeven, Liège, Belgium, 24–28 September, 2012.
[27]F. Louche, P. Dumortier, F. Durodié, and A. Messiaen, "Influence of the blanket shield modules geometry on the operation of the ITER ICRF antenna," Fusion Eng. Des. **88**, 926–929 (2013); in Proceedings of the 27th Symposium On Fusion Technology (SOFT-27), edited by O. Neubauer, R. Koch, P. Mertens, and T. Verhoeven, Liège, Belgium, 24–28 September 2012.
[28]F. Louche, A. Messiaen, P. Dumortier, F. Durodié, R. Koch, and P. Lamalle, "Eigenmode analysis of the iter icrf antenna plug and electrical solution to the grounding of the antenna," Nucl. Fusion **49**, 065025 (2009).
[29]F. Louche and V. Kyrytsya, "CIA report on coupling and grounding," private communication (ITER organization IDM report, 2012).
[30]S. Ramo, J. R. Whinnery, and T. Van Duzer, *Fields and Waves in Communication Electronics* (John Wiley & Sons, NY, 1965).
[31]F. E. Borgnis and C. H. Papas, *Handbuch der Physik* (Springer, Berlin, Heidelberg, NY, 1958), Vol. Electromagnetic Waves.
[32]S. A. Schelkunoff, *Handbuch der Physik* (Van Nostrand, New York, 1943), Vol. Electromagnetic Waves, Chap. 8.